J|A|C|S COMMUNICATIONS

Published on Web 09/07/2010

Top-Down Fabrication of α-Fe_2O_3 Single-Crystal Nanodiscs and Microparticles with Tunable Porosity for Largely Improved Lithium Storage Properties

Jun Song Chen,[†] Ting Zhu,[†] Xiao Hua Yang,[‡] Hua Gui Yang,[‡] and Xiong Wen Lou*,[†]

School of Chemical and Biomedical Engineering, Nanyang Technological University, 70 Nanyang Drive, Singapore 637457, and Key Laboratory for Ultrafine Materials of Ministry of Education, School of Materials Science and Engineering, East China University of Science & Technology, 130 MeiLong Road, Shanghai 200237, China

Received July 8, 2010; E-mail: xwlou@ntu.edu.sg

Abstract: In this work, we report a facile top-down approach to fabricate uniform single-crystal α-Fe_2O_3 nanodiscs via selective oxalic acid etching. Phosphate ions are employed as a capping agent to control the etching to along the [001] direction. We also show that α-Fe_2O_3 melon-like microparticles with contrasting textural properties can be generated using the same approach. The etched particles exhibit a much larger total pore volume and average pore size compared to the pristine ones, thus serving as the possible origin for their greatly enhanced capacity retention when tested as potential anode materials for lithium-ion batteries.

Hematite (α-Fe_2O_3) is a stable form of iron oxides, which has been widely used in many fields such as biotechnology,[1,2] catalysis,[3] pigment,[4,5] and lithium-ion batteries.[3,6−11] Based on a hexagonal close packing of O atoms with Fe atoms occupying 2/3 of the octahedral sites,[3] α-Fe_2O_3 has been engineered into a wide range of nanostructures, including uniform nanocrystals[1] and nanocubes,[12,13] one-dimensional spindle-like structures,[13−15] nanowires,[16,17] nanorods and nanotubes,[9,11,18−21] and hollow[6,10,22,23] as well as other hierarchical nanostructures.[3,8,24,25] It also serves as an active component in complex nanocomposites.[2,15,26−31] Most of the above nanostructures have been synthesized by traditional hydrothermal methods, while other strategies involving oxidative processes[16,32] have also been demonstrated. However, well-defined two-dimensional (2D) nanocrystals of α-Fe_2O_3 have hardly been synthesized before.[4,7,13]

In this communication, we report a top-down approach to fabricate 2D α-Fe_2O_3 single-crystal nanodiscs and porous α-Fe_2O_3 microparticles via a controlled $H_2C_2O_4$ etching process. Oxalic acid ($H_2C_2O_4$) is considered as the most effective agent to dissolve the iron oxide contaminant in minerals.[33,34] Generally, the reaction involved in the dissolution process is shown below:[33] $5H_2C_2O_4 + Fe_2O_3 \rightarrow 2H_2Fe(C_2O_4)_2 + 3H_2O + 2CO_2$. Unlike strong inorganic acids like HCl and HNO_3, $H_2C_2O_4$ is more environmentally benign, and its complexing reaction with iron oxides is more gentle, thus granting better control over the etching process.

We first show that presynthesized single-crystalline α-Fe_2O_3 nanocrystals can be fabricated into uniform nanodiscs by using $H_2C_2O_4$ as the etchant without affecting the original crystallinity. Phosphate ions ($H_2PO_4^-$) are also employed in the current system as a capping agent which allows the etching to proceed favorably along one particular direction. In addition to shape sculpture, our approach is also used to tailor the porosity of microstructures starting with much larger α-Fe_2O_3 melon-like microparticles. We further show that as-obtained porous α-Fe_2O_3 microstructures manifest a significantly improved cycling stability for reversible lithium storage. This is consistent with a generally accepted strategy of using hollow/porous structures to improve the cycling stability of metal oxide based anodes for lithium-ion batteries.[35−38]

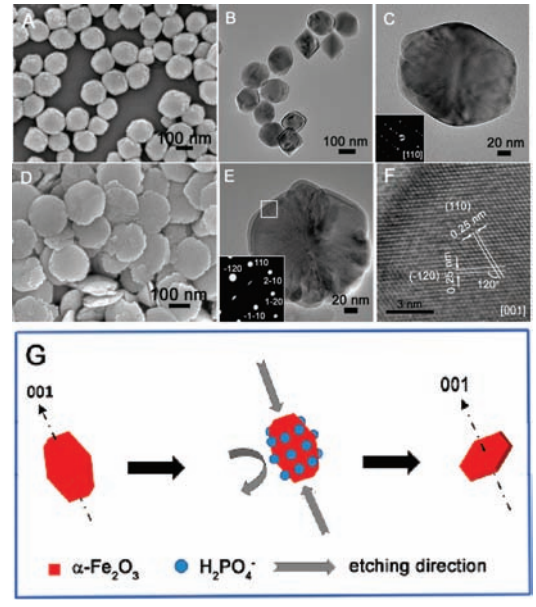

Figure 1. FESEM image (A) and TEM images (B, C) of the α-Fe_2O_3 nanocrystals before etching. FESEM image (D) and TEM image (E) of the α-Fe_2O_3 nanodiscs obtained after etching. (F) High resolution TEM image of the region marked by white square in (E). The insets in (C) and (E) are SAED patterns of the corresponding sample. (G) Schematic illustration of the etching process.

Figure 1A−C show morphologies of the presynthesized α-Fe_2O_3 nanocrystals before etching. Despite having a relatively uniform size distribution (Figure S1A), these α-Fe_2O_3 nanocrystals do not show a well-defined shape. Their single-crystal nature is confirmed by selected-area electron diffraction (SAED) analysis (Figure 1C, inset). Figure 1D depicts a scanning electron microscopy (SEM) image of the α-Fe_2O_3 nanodiscs obtained after being etched for 42 h. It is apparent that the starting nearly isotropic nanocrystals have been transformed into nanodiscs with a relatively uniform size distribution. These nanodiscs are ∼150 nm in diameter and tens of nanometers in thickness (see also Figure S1B) and are generally round or polygonal in shape. Figure 1E shows a transmission electron microscopy (TEM) image of a single nanodisc. From the SAED pattern (Figure 1E, inset) of a perfect hexagonal spot pattern, and the high resolution TEM image (Figure 1F) showing two sets of clear lattice fringes with the same interplanar distance of 0.25 nm at an angle of 60°, it can be concluded that the nanodiscs are

[†] Nanyang Technological University.
[‡] East China University of Science & Technology.

10.1021/ja1060438

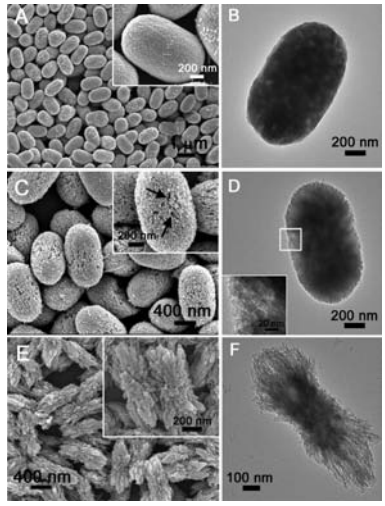

Figure 2. FESEM images of samples I (A), II (C), and III (E) and TEM images of samples I (B), II (D), and III (F). The insets in (A), (C), and (E) are the magnified images of the corresponding sample, and that in (D) shows the magnified image of the region marked by the white square.

lying on their (001) planes.[19] X-ray diffraction (XRD) analysis (Figure S2) confirms that both the nanocrystals and nanodiscs are phase-pure α-Fe_2O_3.

In order to understand the etching process, a control experiment without $H_2PO_4^-$ ions added was carried out while keeping other conditions unaltered. Platelet-like nanostructures with varied shapes and divergent thickness are formed, reflecting the crucial role of $H_2PO_4^-$ ions during the reaction. Based on the above observations, the etching process can be illustrated in Figure 1G. Because of their strong affinity to the (110) planes, phosphate ions will first adsorb on the lateral surfaces of these α-Fe_2O_3 nanocrystals mainly through the formation of binuclear complexes,[19] which prevents $H_2C_2O_4$ molecules from attacking the particles through these regions. As a result, etching is largely favorable at the two ends of the nanocrystals, where the adsorption of phosphate ions is minimized due to the much lower affinity. After prolonged reaction for a carefully controlled duration, a uniform disk structure will be formed as a consequence of the preferred etching along the [001] direction. The results obtained from the time-serial analysis are in support of the proposed mechanism (Figure S3), and the etching is shown to be a controllable process to a certain extent, where α-Fe_2O_3 nanodiscs with tunable thickness and edge roughness can be readily obtained simply by adjusting the etching duration.

This type of uniform disk-like structure can also be generated by etching the quasi nanocubes with ~100 or ~500 nm in size (Figure S4). We can probably generalize the understanding that regardless of the morphology of the original isotropic single-crystal nanocrystals, uniform nanodiscs will be produced with the help of the $H_2PO_4^-$ ions which guarantee that the etching proceeds favorably along the [001] direction. On the other hand, rod-like α-Fe_2O_3 nanostructures can be fabricated by applying this etching method to highly anisotropic α-Fe_2O_3 nanospindles (Figure S5). It is therefore believed that via proper modification of the etching behavior, such as introducing a different capping agent, the present top-down approach can be further expanded to produce other nanomaterials with various features.

We next demonstrate the versatility of our approach by tuning the porosity of α-Fe_2O_3 microparticles. Figure 2A and B show the morphology of these presynthesized "melon-like" particles (designated as sample I), which are quite uniform with a length of ~1.5 μm and a diameter of ~800 nm. The surface of these microparticles is generally smooth, except for some attached fine nanoparticles (Figure 2A, inset). After etching for 36 h, the surface of these microparticles becomes noticeably rougher (Figure 2C and D) while the overall melon-like shape is unchanged (designated as sample II). It can be observed from the magnified image (Figure 2C, inset) that some large pores (indicated by black arrows) have been created at the equatorial regions of the particles, which can be better revealed by the much lighter contrast under TEM (Figure 2D, inset). When the etching is prolonged to 42 h, the morphology of the particles changes dramatically into a dumbbell-like structure composed of nanorods (Figure 2E; designated as sample III). From the TEM image (Figure 2F), it is apparent that the middle portion of the particles becomes much narrower (compare Figure 2 D and F) with an ~300 nm width, while the two ends are etched to a greater extent with the presence of a large amount of porosity. The N_2 sorption measurement (Figure S6) confirms that the total pore volume and average pore size of the particles increase considerably with increasing etching time (Table 1). Although the structure of the melon-like particles changes substantially during the etching process, the uniformity is not affected and no collapse is observed (Figure S7). Moreover, XRD analysis (Figure S8) shows that the crystal phase of the particles is not altered, although the peak intensity decreases significantly after 42 h of etching.

Table 1. Key Parameters of Samples I, II, and III

Sample No.	Etching Time (h)	Surface Area ($m^2\ g^{-1}$)	Total Pore Volume ($cm^3\ g^{-1}$)	Average Pore Size (nm)
I	0	38.9	0.0342	0.352
II	36	44.2	0.088	7.971
III	42	51.5	0.194	15.02

The important role of phosphate ions is again confirmed by a similar control experiment. In the absence of $H_2PO_4^-$ ions, neither preferential etching site nor structural evolution is observed. Thus, the etching process could be described as follows: initially, phosphate ions, as an effective capping agent, will favorably attach to the two ends of the melon-like particles. Hence the etching reaction mainly takes place at the equatorial regions. As the etching proceeds, the generated Fe^{2+} ions by reduction, probably together with the presence of light, will greatly enhance the etching kinetics due to an autocatalytic effect on Fe^{3+} detachment.[33,34] Thus, the etching will no longer be limited to the central region by the adsorbed phosphate ions. Instead, it spreads to the two ends of the particles and becomes much faster. This leads to the dramatic morphological change and significant increase in porosity of the microparticles.

We further evaluate the electrochemical lithium storage capability of these α-Fe_2O_3 microparticles with contrasting textural properties as potential anode materials for lithium-ion batteries. Both samples I and II show similar charge−discharge voltage profiles in the first cycle (Figure S9), which are consistent with previously reported data.[3,6,8−10] Figure 3 shows the comparative cycling performance of two samples at a current rate of 200 mA g^{-1}. Apparently, sample II exhibits a significantly improved cyclic capacity retention compared to sample I. At the end of 100 charge−discharge cycles, a reversible capacity of 662 mA h g^{-1} can still be retained by sample II, while sample I is only able to deliver a much lower capacity of 341 mA h g^{-1}. With the similarities in crystallinity, specific surface area, size, and morphology of these two samples taken into consideration, it might be reasonable to attribute the much better capacity retention shown by sample II to its higher porosity created by the controlled etching process,[3] which effectively buffers the volume change during the charge−discharge processes.

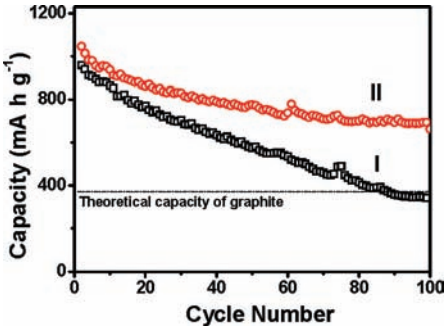

Figure 3. Comparative cycling performance showing the discharge capacities of samples I and II at a current rate of 200 mA g^{-1} from 0.05 to 3 V.

In summary, we have demonstrated a facile top-down approach to fabricate uniform single-crystal α-Fe_2O_3 nanodiscs through a controlled oxalic acid etching process at room temperature. The selective etching along the [001] direction is made possible by employing phosphate ions as a biased capping agent. We further illustrate the versatility of our approach by creating α-Fe_2O_3 microsized melon-like particles with contrasting textural properties. The total pore volume and average pore size of the microparticles can be readily tuned by varying the etching time. When evaluated for their possible use in lithium-ion batteries, the etched microparticle sample with a much higher total pore volume exhibits a significantly improved capacity retention compared to the pristine one. Through modifying the etching conditions, such as the capping agent used or the starting nanostructures, we believe that this interesting top-down approach might be extended to fabricate other nanomaterials with unique structures as well as advanced physical and/or chemical properties.

Acknowledgment. The authors are grateful to the Ministry of Education (Singapore) for financial support through the AcRF Tier-1 funding (RG 63/08, M52120096).

Supporting Information Available: Detailed experimental procedures, more TEM and SEM images, XRD patterns, charge−discharge voltage profiles, N_2 adsorption−desorption isotherm, and complete ref 19. This material is available free of charge via the Internet at http://pubs.acs.org.

References

(1) Park, J.; An, K. J.; Hwang, Y. S.; Park, J. G.; Noh, H. J.; Kim, J. Y.; Park, J. H.; Hwang, N. M.; Hyeon, T. *Nat. Mater.* **2004**, *3*, 891.
(2) Park, H. Y.; Schadt, M. J.; Wang, L.; Lim, I. I. S.; Njoki, P. N.; Kim, S. H.; Jang, M. Y.; Luo, J.; Zhong, C. J. *Langmuir* **2007**, *23*, 9050.
(3) Zeng, S. Y.; Tang, K. B.; Li, T. W.; Liang, Z. H.; Wang, D.; Wang, Y. K.; Qi, Y. X.; Zhou, W. W. *J. Phys. Chem. C* **2008**, *112*, 4836.
(4) Wang, J.; White, W. B.; Adair, J. H. *J. Am. Ceram. Soc.* **2005**, *88*, 3449.
(5) Cornell, R. M.; Schwertmann, U. *The Iron Oxides. Structure, Properties, Reactions, Occurrence and Uses*; VCH: Weinheim, 1996.
(6) Zhou, J. S.; Song, H. H.; Chen, X. H.; Zhi, L. J.; Yang, S. Y.; Huo, J. P.; Yang, W. T. *Chem. Mater.* **2009**, *21*, 2935.
(7) Nuli, Y. N.; Zhang, P.; Guo, Z. P.; Liu, H. K. *J. Electrochem. Soc.* **2008**, *155*, A196.
(8) Pan, Q. T.; Huang, K.; Ni, S. B.; Yang, F.; Lin, S. M.; He, D. Y. *J. Phys. D: Appl. Phys* **2009**, *42*, 015417.
(9) Wu, C. Z.; Yin, P.; Zhu, X.; OuYang, C. Z.; Xie, Y. *J. Phys. Chem. B* **2006**, *110*, 17806.
(10) Kim, H. S.; Piao, Y.; Kang, S. H.; Hyeon, T.; Sung, Y. E. *Electrochem. Commun.* **2010**, *12*, 382.
(11) Chen, J.; Xu, L. N.; Li, W. Y.; Gou, X. L. *Adv. Mater.* **2005**, *17*, 582.
(12) Zheng, Y. H.; Cheng, Y.; Wang, Y. S.; Bao, F.; Zhou, L. H.; Wei, X. F.; Zhang, Y. Y.; Zheng, Q. *J. Phys. Chem. B* **2006**, *110*, 3093.
(13) Sugimoto, T.; Muramatsu, A.; Sakata, K.; Shindo, D. *J. Colloid Interface Sci.* **1993**, *158*, 420.
(14) Zhang, W. M.; Wu, X. L.; Hu, J. S.; Guo, Y. G.; Wan, L. J. *Adv. Funct. Mater.* **2008**, *18*, 3941.
(15) Lou, X. W.; Yuan, C. L.; Archer, L. A. *Adv. Mater.* **2007**, *19*, 3328.
(16) Fu, Y. Y.; Chen, J.; Zhang, H. *Chem. Phys. Lett.* **2001**, *350*, 491.
(17) Fu, Y. Y.; Wang, R. M.; Xu, J.; Chen, J.; Yan, Y.; Narlikar, A.; Zhang, H. *Chem. Phys. Lett.* **2003**, *379*, 373.
(18) Jia, C. J.; Sun, L. D.; Yan, Z. G.; You, L. P.; Luo, F.; Han, X. D.; Pang, Y. C.; Zhang, Z.; Yan, C. H. *Angew. Chem., Int. Ed.* **2005**, *44*, 4328.
(19) Jia, C. J.; et al. *J. Am. Chem. Soc.* **2008**, *130*, 16968.
(20) Mandal, S.; Müller, A. H. E. *Mater. Chem. Phys.* **2008**, *111*, 438.
(21) Jia, C. J.; Sun, L. D.; Yan, Z. G.; Pang, Y. C.; You, L. P.; Yan, C. H. *J. Phys. Chem. C* **2007**, *111*, 13022.
(22) Piao, Y.; Kim, J.; Bin Na, H.; Kim, D.; Baek, J. S.; Ko, M. K.; Lee, J. H.; Shokouhimehr, M.; Hyeon, T. *Nat. Mater.* **2008**, *7*, 242.
(23) Lu, J.; Chen, D. R.; Jiao, X. L. *J. Colloid Interface Sci.* **2006**, *303*, 437.
(24) Gou, X. L.; Wang, G. X.; Kong, X. Y.; Wexler, D.; Horvat, J.; Yang, J.; Park, J. *Chem.—Eur. J.* **2008**, *14*, 5996.
(25) Zheng, Z.; Chen, Y. Z.; Shen, Z. X.; Ma, J.; Sow, C. H.; Huang, W.; Yu, T. *Appl. Phys. A: Mater. Sci. Process.* **2007**, *89*, 115.
(26) Zhang, D. F.; Sun, L. D.; Jia, C. J.; Yan, Z. G.; You, L. P.; Yan, C. H. *J. Am. Chem. Soc.* **2005**, *127*, 13492.
(27) Niu, M. T.; Huang, F.; Cui, L. F.; Huang, P.; Yu, Y. L.; Wang, Y. S. *ACS Nano* **2010**, *4*, 681.
(28) Wang, W. W. *Mater. Res. Bull.* **2008**, *43*, 2055.
(29) Ang, C. Y.; Giam, L.; Chan, Z. M.; Lin, A. W. H.; Gu, H.; Devlin, E.; Papoefthymiou, G. C.; Selvan, S. T.; Ying, J. Y. *Adv. Mater.* **2009**, *21*, 869.
(30) Lou, X. W.; Archer, L. A. *Adv. Mater.* **2008**, *20*, 1853.
(31) Chen, J. S.; Li, C. M.; Zhou, W. W.; Yan, Q. Y.; Archer, L. A.; Lou, X. W. *Nanoscale* **2009**, *1*, 280.
(32) Andreeva, D.; Tabakova, T.; Mitov, I.; Andreev, A. *J. Mater. Sci.: Mater. Electron.* **1991**, *2*, 199.
(33) Lee, S. O.; Tran, T.; Jung, B. H.; Kim, S. J.; Kim, M. J. *Hydrometallurgy* **2007**, *87*, 91.
(34) Veglio, F.; Passariello, B.; Barbaro, M.; Plescia, P.; Marabini, A. M. *Int. J. Miner. Process.* **1998**, *54*, 183.
(35) Lou, X. W.; Archer, L. A.; Yang, Z. C. *Adv. Mater.* **2008**, *20*, 3987.
(36) Lou, X. W.; Li, C. M.; Archer, L. A. *Adv. Mater.* **2009**, *21*, 2536.
(37) Chen, J. S.; Tan, Y. L.; Li, C. M.; Cheah, Y. L.; Luan, D. Y.; Madhavi, S.; Boey, F. Y. C.; Archer, L. A.; Lou, X. W. *J. Am. Chem. Soc.* **2010**, *132*, 6124.
(38) Xiao, W.; Chen, J. S.; Lu, Q.; Lou, X. W. *J. Phys. Chem. C* **2010**, *114*, 12048.

JA1060438